Journal of Alloys and Compounds 859 (2020) 158222

Contents lists available at ScienceDirect

Journal of Alloys and Compounds

journal homepage: www.elsevier.com/locate/jalcom

Microstructure evolution and mechanical properties of commercial pure titanium subjected to rotary swaging

Ao Meng, Xiang Chen*, Jinfeng Nie, Lei Gu, Qingzhong Mao, Yonghao Zhao*

Nano and Heterogeneous Materials Center, School of Materials Science and Engineering, Nanjing University of Science and Technology, Nanjing 210094, China

ARTICLE INFO

Article history:
Received 13 October 2020
Received in revised form 29 November 2020
Accepted 3 December 2020
Available online 10 December 2020

Keywords:
Commercial pure Ti
Rotary swaging
Microstructure evolution
EBSD

ABSTRACT

The wide applications of pure titanium (Ti) are greatly limited by its low strength and hardness. In this paper, we employed an industrial method of rotary swaging (RS) to improve the strength of commercial pure (CP) Ti and uncovered the elementary mechanisms governing microstructural changes under RS. Specifically, the {10-12} extension and {11-22} contraction twins take place in the coarse grains at the early stage of RS deformation, which contributes to the increase of yield strength and moderate ductility. As for the late stage, the twins disappear and are replaced by textured nanostructured grains; meanwhile, there exists a hardness gradient along the radial sample direction. High strain rate RS brings about profuse twins and rapid grain refinement at room temperature in contrast to conventional severe plastic deformation. We rationalize that the high yield strength of CP Ti (up to 955 MPa) is attributed to dislocation, grain boundary and texture strengthening. This result may provide some insights in microstructure-based design of metals with superior mechanical properties subjected to this scalable RS technique.

1. Introduction

Commercially pure (CP) titanium exhibits high biocompatibility and comparable elastic modulus with the bone tissue, which renders it increasingly demanding for medical applications [1–4]. One existing issue is that the coarse-grained (CG) CP Ti displays low strength and poor resistance to wear, being a serious impediment against wider applications [5,6]. Although the strength can be elevated through alloying as exemplified in the traditional Ti-6Al-4V, the alloying elements may release into the human body and unavoidably pose health issues [5]. Therefore, pure titanium with superior mechanical properties would be urgently required.

Rotary swaging (RS) is a widely used industrial method allowing for high-throughput mass production of materials with enhanced mechanical properties. This process enables large hydrostatic stresses and thus facilitates the accumulation of large strain. Recently, the improvement of mechanical properties has been reported in Cu, Al, Mg, W, Ti and their alloys [7–13], ascribed to the development of nanostructured or ultrafine-grained (UFG) structures according to the Hall-Petch relationship [14–20]. For instance, Pachla et al. [12] and Huang et al. [13] pointed out that the strength and ductility of the CP Ti were comparable to those of the Ti-6Al-4V alloy through RS combined with subsequent thermal treatment. Several plastic deformation mechanisms have been identified in the late stage of RS, like grain refinement via formation of grain/subgrains and continuous dynamic recrystallization [12,13]. However, these current experimental results do not yield a satisfactory picture about the elementary mechanisms governing microstructural changes under RS, thus restricting the capability for microstructural design of metals with optimized mechanical properties. The reason for this lack of knowledge is due to unknown aspects regarding the microstructure changes in the early stage of the RS.

With the above issues in mind, the objectives of the present work are twofold as follows. First, a one-step rotary swaging process without thermal treatment will be conducted in an effort to examine the previously overlooked microstructure evolution and deformation mechanisms in the CP Ti. Second, the relationship between microstructure evolution, texture, and mechanical properties of the RS-processed CP Ti will be critically appraised by detailed microstructural analysis.

2. Experiments

2.1. Sample preparation

CP Ti rods of diameter of 30 mm and height of 100 mm (Shaanxi Lianzhong Co., Ltd., China) ingot were used as the starting materials.

* Corresponding authors.
E-mail addresses: xiang.chen@njust.edu.cn (X. Chen), yhzhao@njust.edu.cn (Y. Zhao).

https://doi.org/10.1016/j.jallcom.2020.158222
0925-8388/

Table 1
Chemical compositions of commercial pure titanium alloy studied in this work (mass%).

Elements	Fe	C	N	H	O	Ti
wt%	0.02	0.009	0.007	0.001	0.065	Bal

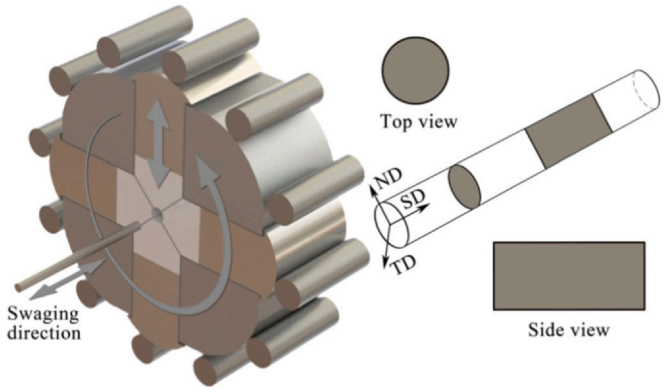

Fig. 1. Schematic illustration of the rotary swaging process and the definition of the sample coordinate system for further microstructural analysis.

Table 2
The sample diameter and corresponding deformation strain of the as-received and RS-processed samples.

Condition	Diameter, mm	True strain
As-received	30.0	0.00
RS 1	24.6	0.40
RS 2	11.0	2.00

Their chemical compositions are given in Table 1. A type of four-die rotary swaging machine (Fig. 1) was utilized to process the CP Ti samples. The principle of its operation is simple as illustrated in Fig. 1. The sample coordinates were defined by the swaging direction (SD), normal direction (ND) and transverse direction (TD). A series of molds were used to reduce the diameter of cross-section from 30 mm to 11 mm (one pass about 0.5 mm) with strain rate ranged from 10 to 10^2 s^1 at the room temperature [21]. Thereafter, typical swaged samples at various true strains were selected for further investigations (see Table 2). The deformation strain is defined as $\varphi = \ln(A_0/A)$ where A_0 and A are the initial and final cross-section area of the Ti samples, respectively [8,10].

2.2. Tensile testing

Flat dog-bone tensile specimens with gauge dimensions of $1.5 \times 2.5 \times 10\ mm^3$ were sectioned by electrical discharge machining (EDM) from the various swaged samples along the swaging direction. All tensile specimens were polished prior to tension using 0.25 µm diamond suspension. The uniaxial tensile samples were tested at room temperature with a universal tensile testing machine (LFM-20, Walter + Baiag, Löhningen, Switzerland) at an initial strain rate of 1×10^{-3} s^{-1}. The tensile tests were repeated at least three times for each specimen.

2.3. Microstructural characterizations

Microstructural characterization was carried out by means of electron back-scattered diffraction (EBSD) and transmission electron microscope (TEM) techniques. Specifically, EBSD mapping was conducted using a high-resolution field emission Carl Zeiss-Auriga-45–66 scanning electron microscope (SEM) equipped with a fully automatic Oxford Instruments Aztec 2.0 EBSD system (Channel 5 software). Two types of metallographic sections were taken from the RS samples, referred to as the top-view and side-view samples. The top-view and side-view samples were prepared in the ND-TD and ND-SD planes of the CP Ti samples, respectively (Fig. 1). The specimens for EBSD characterization were mechanically polished with SiC paper and then electro-polished in an electrolyte containing 90 vol% acetic acid and 10 vol% perchloric acid using a voltage of 35 V and polishing time of 50 s in a Buehler ElectroMet 4 polisher. TEM observations were conducted in an FEI-Tecnai G^2 20 S-TWIN microscope operated at 200 kV. The TEM specimens were prepared by grinding the deformed specimens down to 60 µm thickness and then punched into discs with a diameter of 3 mm and were finally electro-polished to an electron-transparent thickness in an aqueous electrolyte containing 10% perchloric acid, and 90 vol% ethyl alcohol at 20 °C via a twin jet electro-polishing system.

3. Results and discussion

3.1. Microstructure characterization

Fig. 2 shows the top-view and side-view microstructure of the as-received CP Ti. Coarse equiaxed grains with an average size of about 10.7 µm are observed in the inverse pole figure (IPF) map for the top view sample (Fig. 2a). In the side view, the coarse grains are elongated along the SD with comparable grain size (Fig. 2d). The equiaxed grains consist of a large volume fraction of HAGBs and a few LAGBs for the top view (Fig. 2b). There are plenty of LAGBs in the elongated grain interior from the side view. The Kernel Average Misorientation (KAM) measure is used as an index for describing the accumulated local lattice curvature due to rotary swaging. Herein, the 2nd neighboring shell is considered and misorientations larger than 5° are discarded to avoid an artificial effect from adjacent grain boundaries. In the as-received sample, only LAGBs are associated with high KAM values (Fig. 2c and f).

Fig. 3 presents the microstructures of the CP Ti sample subjected to rotary swaging with a deformation strain $\varphi = 0.4$. The grains are elongated from the top view, in contrast to the as-received sample. The occurrence of several twins is clearly observed in the grain interior (Fig. 3a and d). Compared to the as-received sample, the defect density increases in terms of more LAGBs and HAGBs formed in the RS sample (Fig. 3b and e). This is also consistent with the increased KAM values in the LAGBs and HAGBs for each view section (Fig. 3c and f). The interior regions for some large grains remain unaltered according to the blue contours while the twin regions change to the green contours due to strain accumulation.

With increasing strain from 0.4 to 2.0, the grains are substantially refined in the top view section. Plenty of equiaxed grains (117 ± 53 nm) are embedded in the spiral grains (Fig. 4a). In the side view, the grains are elongated and some equiaxed grains are sandwiched in the lamellar structure (Fig. 4d). As seen in Fig. 4b and e, some LAGBs are aggregated in the HAGBs, analogous to the $\varphi = 0.4$ sample. Interestingly, the twinning structure disappears. The corresponding TEM characterization shows the deformed grains with an average size of 117 nm in the top-view section and elongated lamellar structure (averagely 182 nm in thickness) in the side-view section (Fig. 5). It is noted that both lamellar boundaries and grain boundaries are blurry and the grain shape is not discernable. The high dislocation density within the grains may result in high internal stress, as indicated by the red dotted circle in Fig. 5.

The fraction of LAGBs increases with the increasing RS strain according to the misorientation angle distribution (Fig. 6). For instance, the fraction of LAGBs is about 11.3% for the as-received CP Ti on the top view (Fig. 6a), while the fractions of LAGBs at the strain of 0.4 and 2.0 increase to 63.3% and 57.8%, respectively (Fig. 6b and c). The side view section shows the same tendency (Fig. 6d-f). The high fraction of LAGBs may be due to the fact that the dislocations

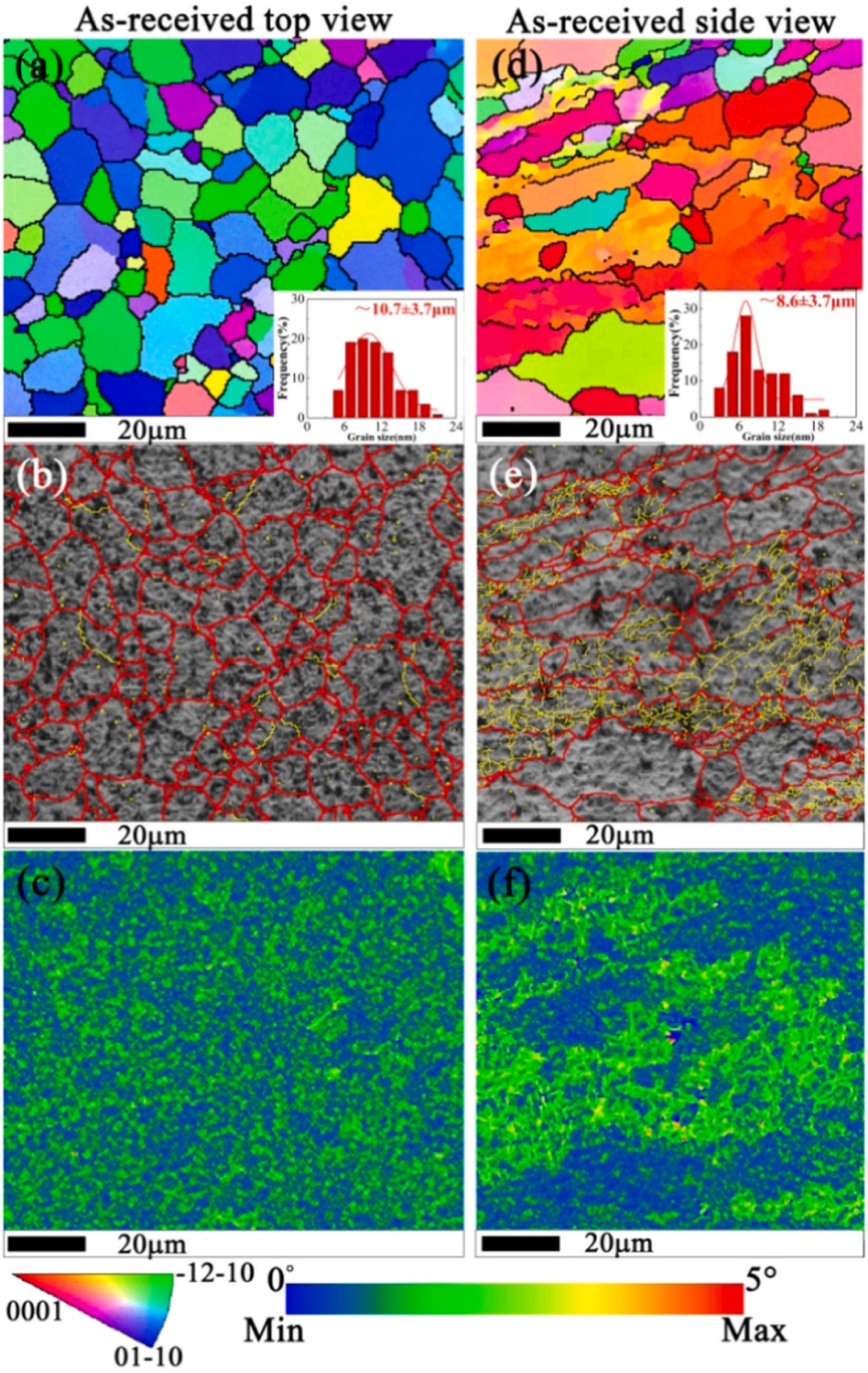

Fig. 2. IPF maps (a and d), EBSD boundary maps (b and e) and KAM maps (c and f) for the top view (a-c) and side view (d-f) sections of the as-received CP Ti sample. The top view is parallel to the swaging direction and the side view is perpendicular to swaging direction. The inserts in (a) and (d) are respective grain size distribution. Red lines in the EBSD boundary maps represent misorientation angle > 15° and yellow lines represent misorientation angle between 2° and 15°.(For interpretation of the references to colour in this figure legend, the reader is referred to the web version of this article.)

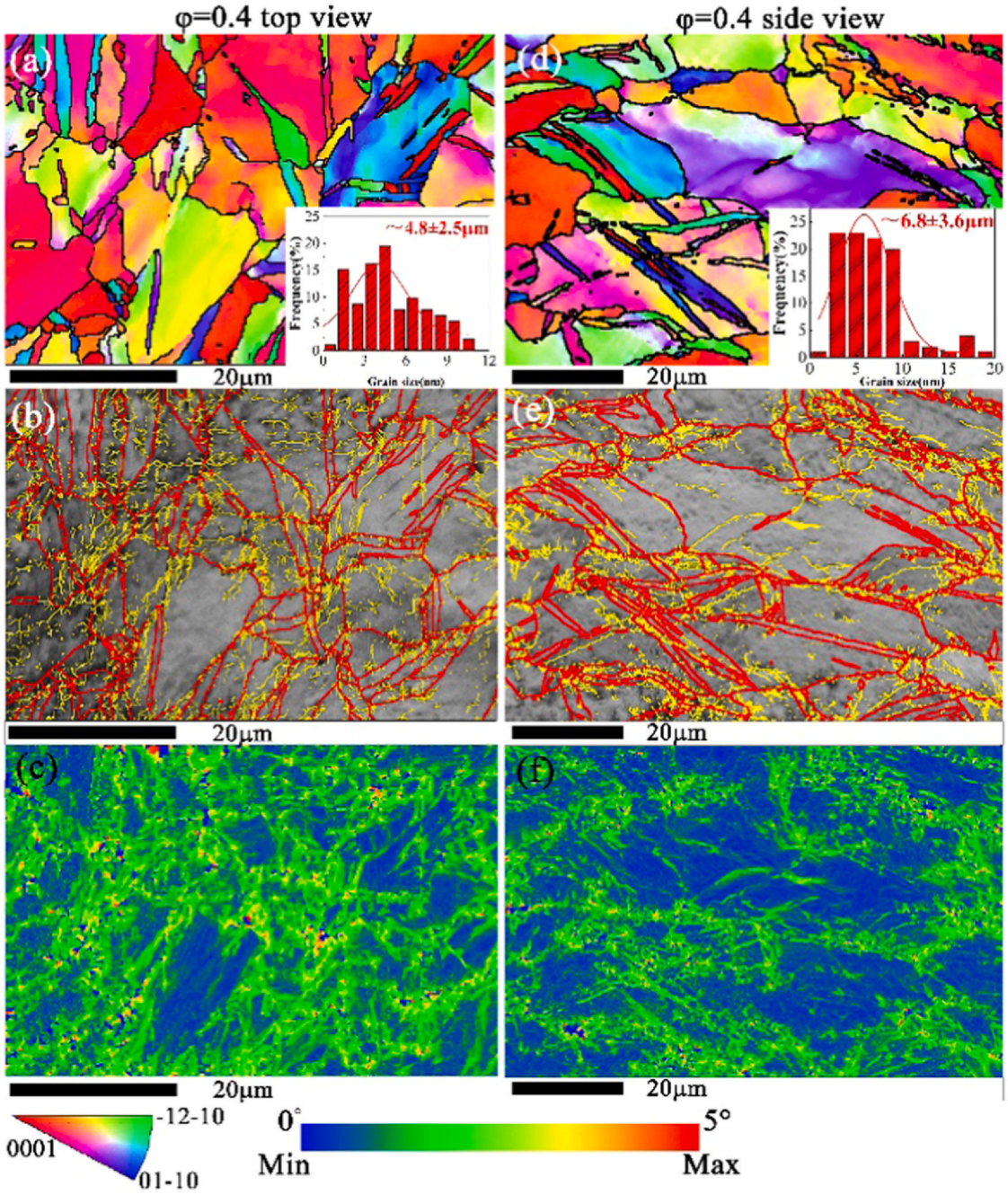

Fig. 3. IPF maps (a and d), EBSD boundary maps (b and e) and KAM maps (c and f) for the top view (a-c) and side view (d-f) sections of the φ = 0.4 sample. The inserts in (a) and (d) are respective grain size distribution. Red lines in (b) and (e) represent misorientation angle > 15° and yellow lines depict misorientation angle between 2° and 15°.(For interpretation of the references to colour in this figure legend, the reader is referred to the web version of this article.)

substructure cannot be annihilated and rearranged. The KAM values are used to evaluate the change in the dislocation density. The KAM distribution shifts to an overall high value for each view section (Fig. 6h-m). Taking the side view as an example, the average KAM value increases from 0.64° in the as-received sample to 1.01° of the φ = 0.4 sample and up to 1.67° for the φ = 2.0 sample (Fig. 6k-m). It can be seen that the misorientations increase when moving from the zones close to the center of the grain to the grain boundaries and the dislocation density increases with the deformation strain (Fig. 3c and f, Fig. 4c and f). This is an indication of the development of plastic gradients within the grains that are accommodated via the formation of geometrically necessary dislocations (GNDs) [22]. These dislocations are mainly assembled close to the grain boundaries so as to accommodate the inhomogeneous deformation between neighboring grains. It was reported that the GND density is the minimum that can accommodate plastic gradients [23]. A rough estimate of the density of GNDs, ρ_{GND}, can be expressed as a function of the accumulated average local misorientation angle, θ, [24]:

$$\rho_{GND} = \frac{\theta}{\mu b} \quad (1)$$

where b is the length of the Burgers vector. Taking b = 0.295 nm for Ti [25], the step μ and the average local misorientation angle θ (KAM) into the Eq. (1), it yields the calculated density for each sample (see Table 3). For instance, the GND density of the as-received CP Ti is 6.88×10^{13} m^{-2} from the top view. The density is about

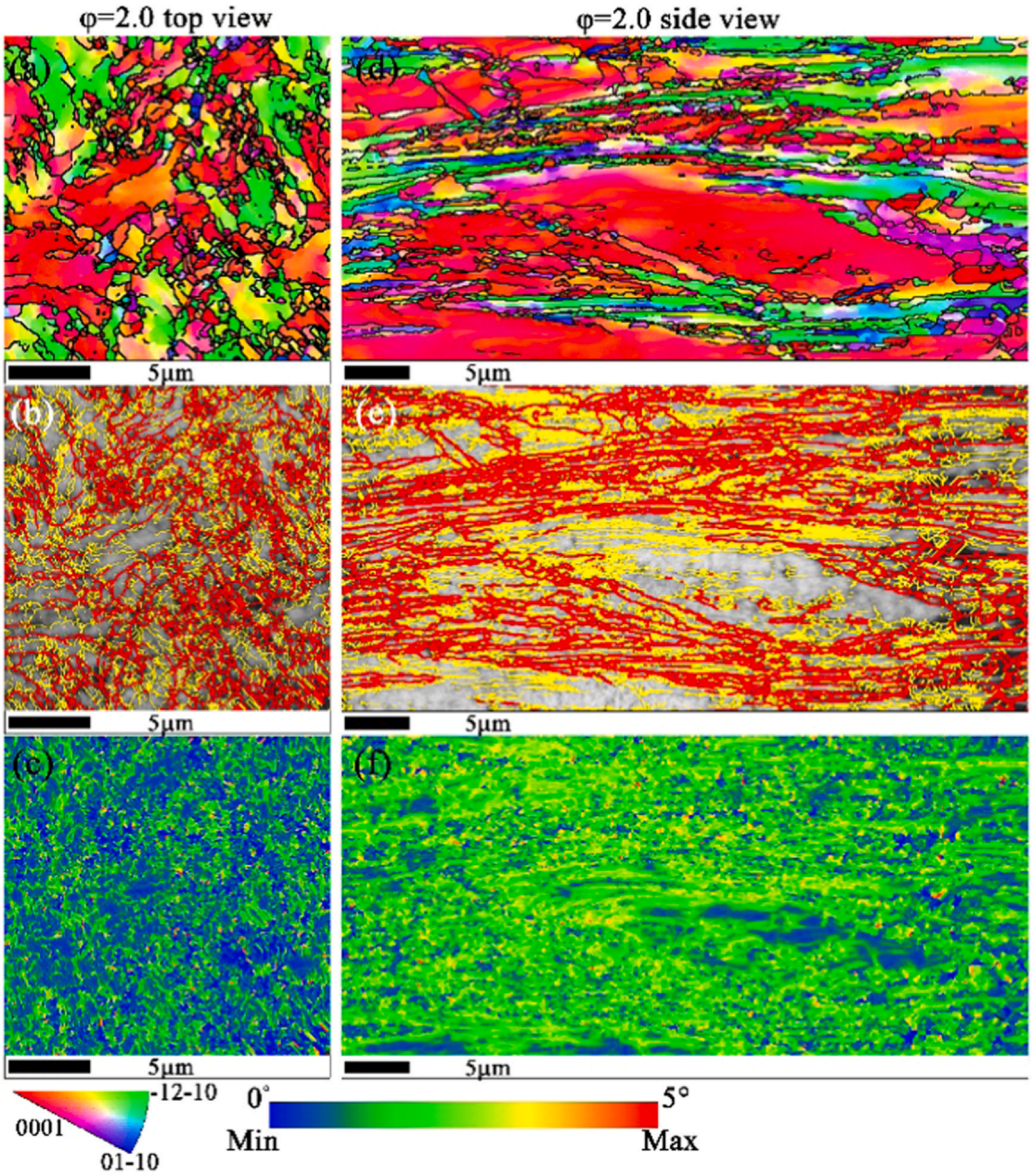

Fig. 4. IPF maps (a and d), EBSD boundary maps (b and e) and KAM maps (c and f) for the top view (a-c) and side view (d-f) sections of the φ = 2.0 sample. Red lines in (b) and (e) depict misorientation angle > 15° and yellow lines represent misorientation angle between 2° and 15°.(For interpretation of the references to colour in this figure legend, the reader is referred to the web version of this article.)

3.82×10^{14} m^{-2} with a deformation strain φ = 0.4 and further increases to 1.44×10^{15} m^{-2} for the sample at a strain of 2.0. It should be noted that the GND density is eventually increased by almost two order of magnitude.

3.2. Twinning and texture evolution

As mentioned above, the twinning structure is observed in the grain interior at a deformation strain φ = 0.4. Misorientation angle distributions are used to identify the twins and their variants (Fig. 6). The peaks at around 65° and 85° have emerged, meaning that {11-22} < 11-2-3 > contraction twin (CT) and {10-12} < -1011 > extension twinning (ET) are formed, respectively (Fig. 6b and e) [26]. It was established that four twinning systems are commonly found in Ti including {11-21} < -1-1126 > , {10-12} < -1011 > , {11-22} < 11-2-3 > and {11-24} < -2-24-3 > , and the first two are extension twins (ETs), while the other two are contraction twins (CTs) [27]. For the four twinning types in Ti, twinning shear τ can be estimated as [28,29]:

$$\tau_{\{11-21\}} = \gamma^{-1} \quad (2)$$

$$\tau_{\{10-12\}} = (\gamma^2 - 3)/\sqrt{3}\gamma \quad (3)$$

$$\tau_{\{11-22\}} = 2(\gamma^2 - 2)/3\gamma \quad (4)$$

$$\tau_{\{11-24\}} = 2(\gamma^2 - 2)/3\gamma \quad (5)$$

where γ is the c/a ratio of Ti (1.587). By using these equations, the twinning shear of $\tau_{\{11-21\}}$, $\tau_{\{10-12\}}$, $\tau_{\{11-22\}}$, $\tau_{\{11-24\}}$ are calculated to be 0.630, 0.175, 0.218 and 0.218, respectively. The lower twinning shear of {10-12} ETs, {11-22} CTs and {11-24} CTs implies that less stress/energy is needed to activate the twinning system. In addition,

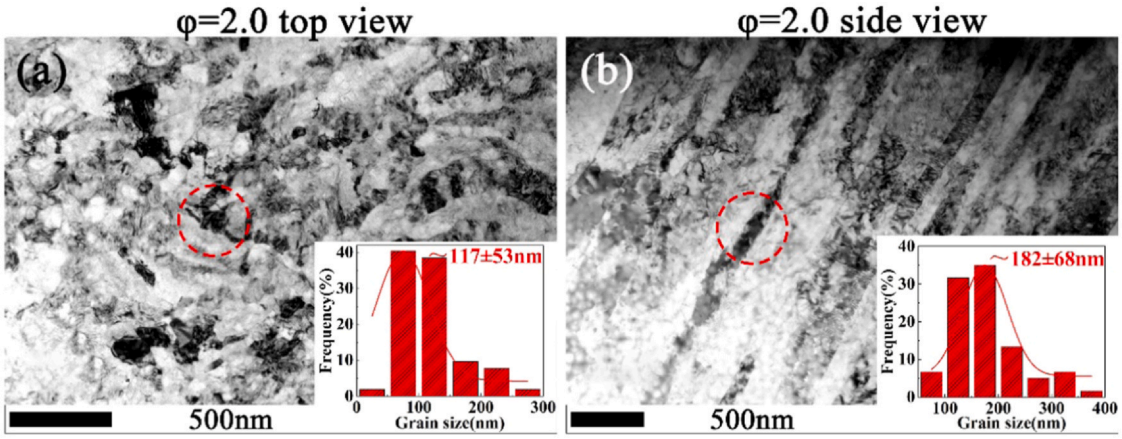

Fig. 5. Typical TEM micrographs showing the microstructure on top view (a) and side view (b) of the deformation degree φ = 2.0 sample, the inserted histograms are grain size distribution and red dotted circles indicate the high dislocation density for each view section.(For interpretation of the references to colour in this figure legend, the reader is referred to the web version of this article.)

activation of twinning is heavily dependent on the included angle between the loading direction and c axial of the grain in the Ti alloys. As a part of Schmid factor analysis, Fig. 7 shows the Schmid factor distribution of the four twinning systems for the as-received sample subjected to RS treatment. The Schmid factor distributions show that {11-21} < -1-126 > twin with an average Schmid factor of 0.452 (Fig. 7a), while {10-12} < -1011 > , {11-22} < 11-2-3 > twin with the average Schmid factor of 0.331, 0.393, respectively (Fig. 7b and c). Though the average Schmid factor of {10-12} < -1011 > and {11-22} < 11-2-3 > twinning systems is lower than {11-21} < -1 -126 > twin system, the twinning shear τ of {10-12} < -1011 > and {11-22}< 11-2-3 > twinning systems is much lower than {11-21} < -1-126 > twin system. Moreover, the ratio of twinning shear and Schmid factor for {10-12} < -1011 > twinning system is 0.529, which is lower than the value 0.555 of {11-22} < 11-2-3 > twinning system. Considering that {11-24} twins were only reported at cryogenic temperature for strain accommodation due to the suppression of dislocation slip [28]. Thus it is understandable that the {10-12} ETs and {11-22} CTs are observed twinning types sustaining the early stage RS deformation at room temperature. The misorientation peak of {10-12} ETs is higher than {11-22} CTs owing to the lower twinning shear of {10-12} ETs. Therefore, a larger volume is required for {10-12} ETs to accommodate the same deformation strain as for {11-22} CTs. It is worth noting that the volume fraction of

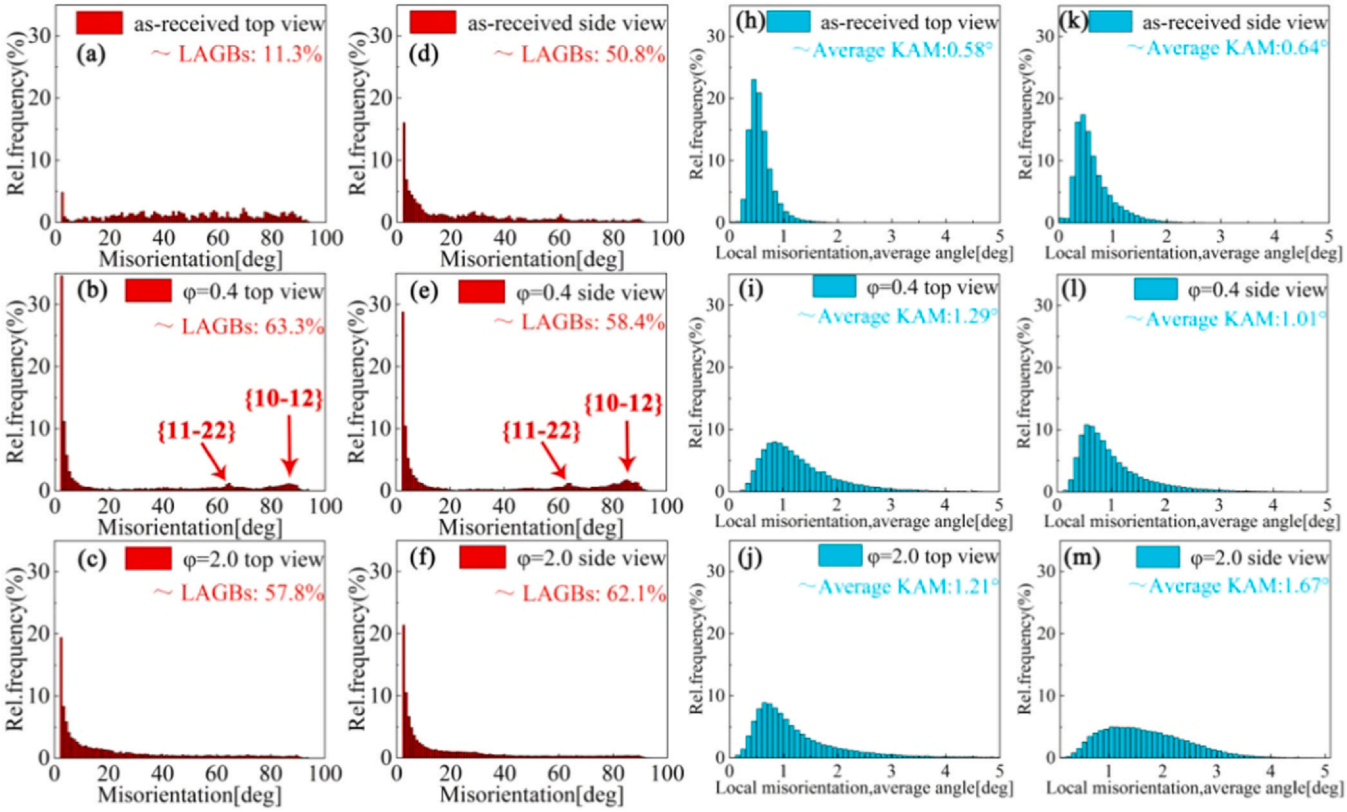

Fig. 6. The histograms of grain boundary misorientation (a-f) and local misorientation (h-m) for the as-received and RS-processed samples: (a and h) top view, (d and k) side view for the as-received sample; (b and i) top view, (e and l) side view for the φ = 0.4 sample; (c and j) top view, (f and m) side view for the φ = 2.0 sample. Corresponding volume fraction of the LAGBs and KAM values are given in the figures as well.

Table 3
The calculated GND density for different samples based on the KAM maps.

Samples	As-received top view	As-received side view	φ = 0.4 top view	φ = 0.4 side view	φ = 2.0 top view	φ = 2.0 side view
θ	0.58°	0.64°	1.29°	1.01°	1.21°	1.67°
μ/μm	0.5	0.4	0.2	0.2	0.05	0.1
ρ^{GND}/m^{-2}	6.88×10^{13}	9.52×10^{13}	3.82×10^{14}	2.99×10^{14}	1.44×10^{15}	1.00×10^{15}

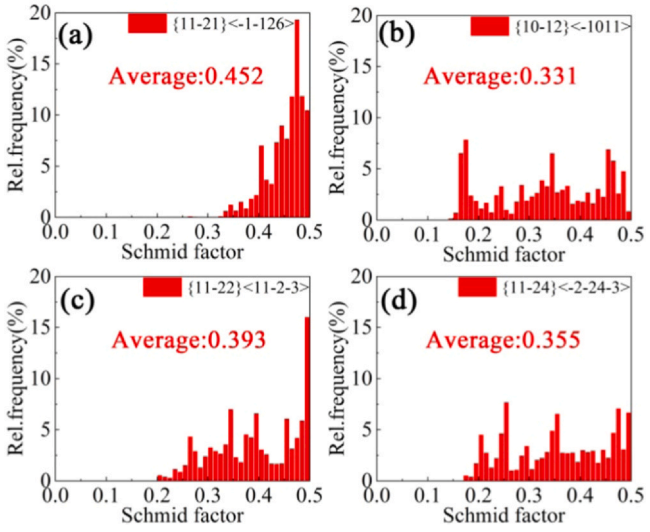

Fig. 7. The Schmid factor distribution of the four twinning systems for the as-received sample subjected to RS treatment: (a) {11-21} < -1-126 > ; (b) {10-12} < -1011 > ; (c) {11-22} < 11-2-3 > ; (d) {11-24} < -2-24-3 > . The average Schmid factors are given in the diagrams and the loading direction is parallel to ND.

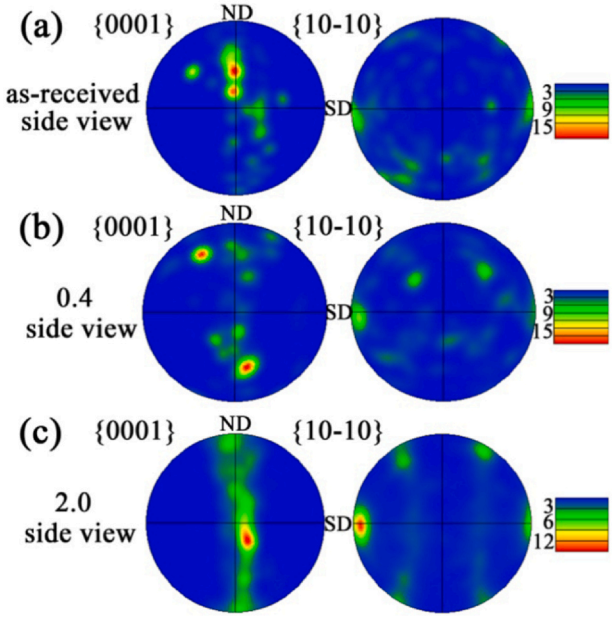

Fig. 8. The ND-SD {0001} and {10-10} pole figures for the (a) as-received sample, (b) φ = 0.4 sample and (c) φ = 2.0 sample. The sample coordinates were defined by the swaging direction (SD), normal direction (ND) and transverse direction (TD).

deformation twins is measured to be 14%, much higher than that under room temperature rolling of pure Ti from a recent investigation [29]. In contrast to conventional severe plastic deformation (SPD), the strain rate during rotary swaging is higher and estimated to be $10–10^2$ s^{-1}, which is favorable for generating twins based on Hollomon equation. This well explains the observed fine and dense twin at the early stage of room temperature RS. With further deformation, the misorientation peaks disappear at the deformation condition φ = 2.0. The fragment of twins is due to interaction between twin boundaries and dislocation. Besides, it was suggested that the deformation twinning becomes more difficult with decreasing grain size but the underlying reason is unclear [30].

The maximum pole intensity of {0001} plane is inclined to ND in the range of 15° ~ 45° and the {10-10} pole figure is distributed loosely for the as-received samples (Fig. 8a). As for the φ = 0.4 samples, the maximum intensity of {0001} plane is about 55° inclined to ND with the tilted angle to SD being about 15° and 30° (Fig. 8b). The {10-10} pole figure is similar to the as-received samples (Fig. 8a and b). The maximum intensity of {0001} plane is parallel to ND and the < 10-10 > fiber texture occurs with respect to SD for the φ = 2.0 sample (Fig. 8c). Such preferred orientation texture for CP Ti is consistent with prior work subjected to swaging and drawing [13,31]. The Schmid factor analysis is further utilized to study the slip activities of the CP Ti samples during RS treatment and tensile deformation (Figs. 9 and 11). The Schmid factor distributions show that {10-11} < 11-23 > slip with an average Schmid factor of 0.434 (Fig. 9d) is most likely to be initiated, while {10-10} < 11-20 > slip with an average Schmid factor of 0.186 (Fig. 9b) is difficult to be facilitated for the as-received CP Ti sample. After RS treatment at the deformation strain φ = 0.4, the average Schmid factor of {10-10} < 11-20 > slip increases to 0.279 (Fig. 9f) and the most active slip system is still {10-11} < 11-23 > , with an average Schmid factor of 0.427 (Fig. 9h). It is known that the Schmid factor indicates the critical resolved shear stress (CRSS) of applied stress ($\sigma_{applied}$) on corresponding slip planes and the $\sigma_{applied}$ needed to stimulate the dislocation can be calculated by the following equation [31]:

$$\sigma_{applied} = \sigma_{CRSS}/m \quad (6)$$

where m is the average Schmid factor of corresponding slip system. It was previously calculated that the CRSS for basal slip, prismatic slip and pyramidal slip are 150 MPa, 30 MPa and 120 MPa, respectively [32]. Thus, we obtain the stress required to activate the slip systems in Ti during deformation (see Tables 4 and 5). It is obvious that the $\sigma_{applied}$ required to stimulate the {10-10} < 11-20 > slip is much lower than that for other dislocations when subjected to the RS process. Therefore, with increasing strain from 0.4 to 2.0, it is reasonable to assume that the highly favorable {10-10} < 11-20 > slip systems would contribute to the formation of < 10-10 > fiber texture and therefore influence the mechanical properties of the CP Ti samples.

3.3. Mechanical properties and strengthening mechanisms

Fig. 10a plots the efficiency of grain refinement as a function of equivalent strain in the RS processing, compared with different SPD techniques in the literature. CR – cold rolling, HE – hydrostatic extrusion, ECAP – equal channel angular pressing, hydrostatic extrusion and KoBo – extrusion through oscillating die. The grain size is refined to 200 nm at the strain φ = 2.7 for cold rolling. As for the HE and KoBo, the grain size is decreased to 500 nm and 650 nm at a strain of 3.2 and 4.2, respectively. Interestingly, the RS processing allows for the rapid grain refinement, which can be seen from the fact that the grain size is refined to 117 nm at the strain φ = 2.0. It can be interpreted that the coarse grain is subdivided by the dense twin lamellar and dislocation slipping and refined to UFGs. The UFGs is

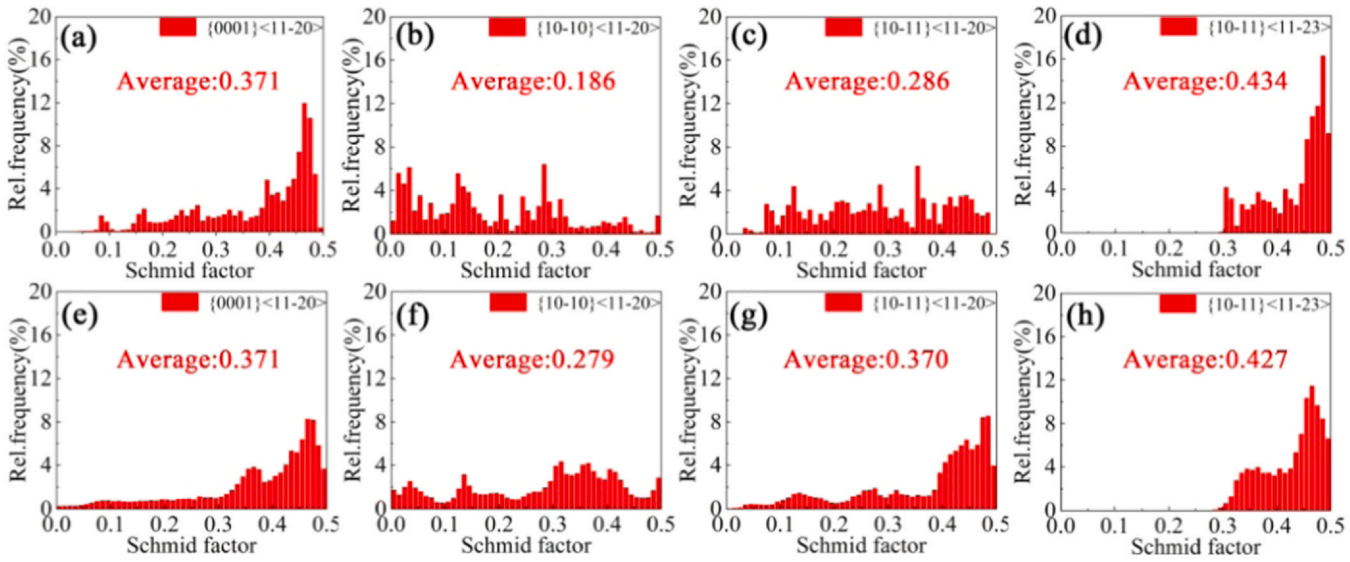

Fig. 9. The Schmid factor distribution of four slip systems for two different deformation strains during RS treatment: (a-d) as-received sample; (e-h) φ = 0.4 sample. The average Schmid factors are given in the diagrams and the loading direction is parallel to ND.

further refined down to nano-grains by slipping at the high strain rate. Fig. 10b and d show the hardness distribution along the radial direction and the tensile properties from the edge to center of the φ = 2.0 sample. As shown in Fig. 10b, the micro-hardness of the as-received CP Ti is ~196 HV. The RS processing brings about a gradient distribution of micro-hardness along the radial sample direction, with a constant value of ~270 HV in the center region, which slightly turns to approximately ~275 HV at the distance of 1.5 mm to the center and then decreases gradually to ~260 HV with the distance increasing to 4.5 mm. The swaged center samples exhibit a higher yield strength but lower ductility (Fig. 10d), which may stem from that the high strain rate could increase the saturated dislocation density and render the strain hardening ability limited. The gradient structure is attributed to the friction between the dies and the Ti sample, resulting in a severe deformed zone in the center region. Fig. 10c displays the typical tensile curves of the RS-processed

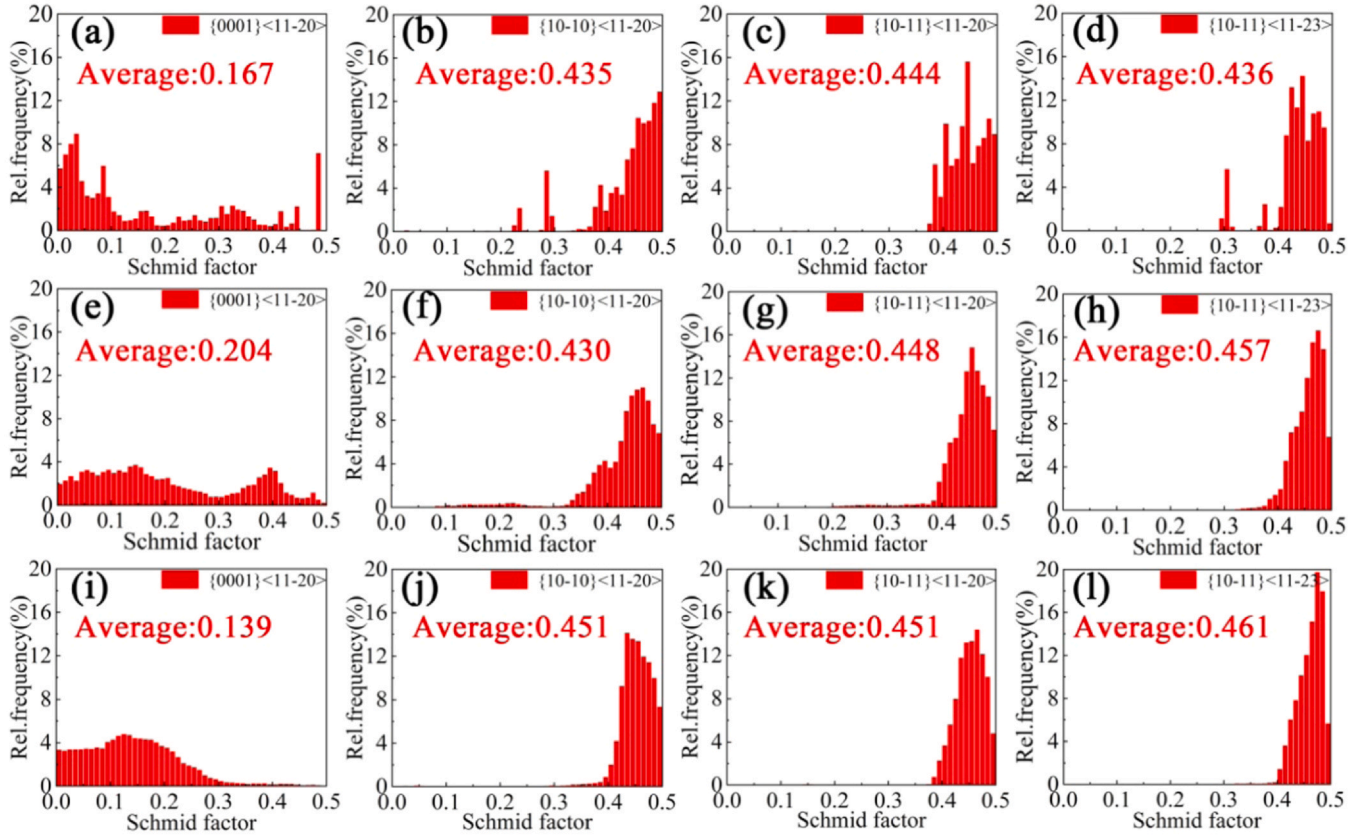

Fig. 11. The Schmid factor distribution of four slip systems for the as-received sample and RS-processed samples during tensile tests: (a-d) as-received sample; (e-h) φ = 0.4 sample; (i-l) φ = 2.0 sample. The average Schmid factors are given in the diagrams and the loading direction is parallel to SD.

Table 4
The applied stress (MPa) needed to active the four slip systems in Ti of different samples during RS treatment.

Samples	{0001}< 11–20 >	{10–10}< 11–20 >	{10–11}< 11–20 >	{10–11}< 11–23 >
As-received	404	161	420	276
φ = 0.4	404	108	324	281

samples compared with the as-received sample. The measured yield strength (YS) and ultimate tensile strength (UTS) of the as-received CP Ti are 417 ± 8 MPa and 549 ± 4 MPa, respectively. For the φ = 0.4 sample, the YS and UTS are 675 ± 20 MPa and 700 ± 12 MPa, respectively. Furthermore, the YS and UTS increase to 953 ± 13 MPa and 976 ± 10 MPa, which are almost two times as high as for the as-received CP Ti. The YS and UTS increases monotonically with the RS strain from 0.4 to 2.0 (Fig. S1a and b), but inevitably leading to a sacrifice of ductility due to the poor strain hardening ability (Fig. 10c and Fig. S1b).

As expected, the strength is substantially elevated, presumably ascribed to Taylor dislocation strengthening and Hall-Petch strengthening as well [14,15]. It is reasonable to assume grain boundary and dislocation strengthening play a crucial role, as the grain size is decreased from 10.7 μm to 117 nm (top view, Figs. 2a and 5a) and the KAM value increases from 0.64 to 1.67. In addition, when the loading direction is parallel to the SD, it is highly favorable for the prismatic slip systems {10-10} < 11-20 > with an average Schmid factor of 0.451 (Fig. 11j) and lower applied stress of 67 MPa (Table 5), but unfavorable for the basal slip {0001} < 11-20 > with Schmid factor of 0.139 (Fig. 11i) and higher applied stress of 1079 MPa (Table 5). This result is analogous to RS-processed CP Ti followed by annealing treatment [13]. The grains that are most favorably orientated for prismatic slip can be deformed at lower values of applied stress. Localization of plastic slip within these grains results in local strain hardening, in turn leading to the increase of the flow stress. Thus, the strength of deformation condition φ = 2.0 is 955 MPa, which is much higher than the strength 417 MPa of the as-received CP Ti. After RS treatment of strain φ = 2.0, dislocation slip is further to accommodate the strain, resulting in high dislocation density generated in the small grain size (117 nm), with the LAGBs percentages of 62.1% (Fig. 6f). The ductility is decreased to one third of the as-received sample, because there is no sufficient site for continuous dislocation gliding and dislocation accumulation.

For the as-received CP Ti and φ = 0.4 samples, they share similar grain size, texture and {10-10} < 11-20 > prismatic slip systems (Fig. 11a-h and Table 5), but the yield strength of φ = 0.4 sample is higher than the as-received materials. This primarily stems from Taylor dislocation strengthening, which can be seen that the GND density increases from 9.52×10^{13} m^{-2} to 2.99×10^{14} m^{-2} with a deformation strain φ = 0.4. Another reason is the deformation twins with a volume fraction of about 14% in the grain interior (Fig. 3b and e), which can serve as obstacles in prohibiting dislocation motion. Besides, lower density of pre-existing dislocation with larger grain size is beneficial for work hardening. Consequently, the tensile ductility of the φ = 0.4 sample is superior to that of the φ = 2.0 sample.

In contrast to the reported RS process combined with thermal treatment, our study assesses the potential of one-step RS in improving the mechanical properties of CP Ti. Obviously, grain boundaries, dislocations, twins, and texture evolve in the different stages of this cost-effective technique, contributing to the enhanced mechanical properties and thereby enabling promising utilization of pure Ti for medical applications.

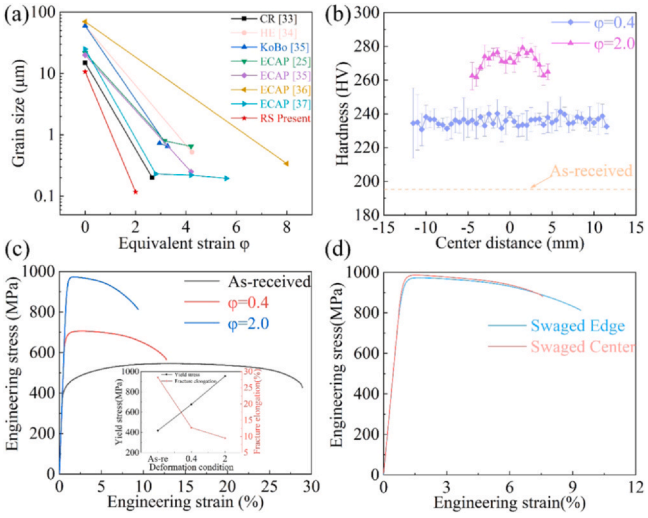

Fig. 10. (a) The resultant grain size of pure Ti as a function of equivalent strain of different SPD treatment [33–37]; (b) The Vickers micro-hardness measured from edge to center in the top view along the TD of the RS-processed CP Ti with the different strain; (c) Engineering stress-strain curves of different deformation strain level, the inserted histogram is statistical value of yield stress and fracture elongation of different deformation condition; (d) Engineering stress-strain curves of the swaged φ = 2.0 sample at the edge and center region.

4. Conclusions

In summary, CP Ti was plastically deformed using one-step rotary swaging to different deformation degrees to examine the previously overlooked microstructure evolution, deformation mechanisms and their impact on the resulting mechanical properties. The main conclusions can be drawn as follows:

(1) The {10-12} extension and {11-22} contraction twins take place in the coarse grains at the early stage of RS deformation, which contributes to the increase of yield strength and moderate ductility.
(2) As for the late stage, the twins disappear and are replaced by textured nanostructured grains with very high strength (up to 955 MPa). We rationalize that the combination of dislocation, grain boundary and texture strengthening is responsible for the high strength of CP Ti in the late stage of RS.
(3) High strain rate RS brings about profuse twins and rapid grain refinement at room temperature in contrast to conventional severe plastic deformation techniques. Taking into account the low-cost and scalable process, we anticipate that the utilization

Table 5
The applied stress (MPa) needed to active the four slip systems in Ti of different samples during tensile tests.

Samples	{0001}< 11–20 >	{10–10}< 11–20 >	{10–11}< 11–20 >	{10–11}< 11–23 >
As-received	898	69	270	275
φ = 0.4	735	70	268	263
φ = 2.0	1079	67	266	260

of bulk CP-Ti with unprecedented strength will be significantly accelerated in the field of medical applications.

CRediT authorship contribution statement

Ao Meng: Rotary swaging experiments, Writing - original draft and revision, EBSD and TEM experiments, Methodology. **Xiang Chen**: Supervision, Writing - original draft, Writing - review & editing, Validation, Conceptualization. **Jinfeng Nie**: EBSD and TEM analysis. **Lei Gu**: EBSD experiments. **Qingzhong Mao**: Rotary swaging experiments. **Yonghao Zhao**: Conceived and designed this study, Supervision, Funding acquisition.

Declaration of Competing Interest

The authors declare that they have no known competing financial interests or personal relationships that could have appeared to influence the work reported in this paper.

Acknowledgements

Y.H. Zhao acknowledges financial supports from the National Key Research and Development Program of China (Grant No. 2017YFA0204403), National Natural Science Foundation of China (Grant No. 51971112 and 51225102) and the Fundamental Research Funds for the Central Universities (Grant No. 30919011405). X. Chen would like to acknowledge financial supports from the Natural Science Foundation of Jiangsu Province, China (Grant No. BK20200475). The authors are thankful for the technical support from Jiangsu Key Laboratory of Advanced Micro&Nano Materials and Technology, and the Materials Characterization Facility of Nanjing University of Science and Technology.

Appendix A. Supporting information

Supplementary data associated with this article can be found in the online version at doi:10.1016/j.jallcom.2020.158222.

References

[1] H.J. Rack, J.I. Qazi, Titanium alloys for biomedical applications, Mater. Sci. Eng. C 26 (2006) 1269–1277.
[2] N. Poondla, T.S. Srivatsan, A. Patnaik, M. Petraroli, A study of the microstructure and hardness of two titanium alloys: commercially pure and Ti-6Al-4V, J. Alloy. Compd. 486 (2009) 162–167.
[3] M. Niinomi, M. Nakai, J. Hidea, Development of new metallic alloys for biomedical applications, Acta Biomater. 8 (2012) 3888–3903.
[4] Z.W. Huang, Y. Cao, J.F. Nie, H. Zhou, Y.S. Li, Microstructures and mechanical properties of commercially pure Ti processed by rotationally accelerated shot peening, Materials 11 (2018) 366.
[5] V.V. Stolyarov, Y.T. Zhu, T.C. Lowe, R.Z. Valiev, Microstructure and properties of pure Ti processed by ECAP and cold extrusion, Mater. Sci. Eng. A. 303 (2001) 82–89.
[6] E.H. Shima, G.H. Cao, L.C. Zhang, Nanoindentation study of mechanical properties of Ti based alloys with Fe and Ta additions, J. Alloy. Compd. 692 (2017) 892–897.
[7] A.H. Huang, Y.F. Wang, M.S. Wang, L.Y. Song, Y.S. Lib, L. Gao, C.X. Huang, Y.T. Zhu, Optimizing the strength, ductility and electrical conductivity of a Cu-Cr-Zr alloy by rotary swaging and aging treatment, Mater. Sci. Eng. A 746 (2019) 211–216.
[8] M.A. Abdulstaar, E.A. El-Danaf, N.S. Waluyo, L. Wagner, Severe plastic deformation of commercial purity aluminum by rotary swaging: microstructure evolution and mechanical properties, Mater. Sci. Eng. A 565 (2013) 351–358.
[9] L. Kunčická, R. Kocich, C. Hervoches, A. Macháčková, Study of structure and residual stresses in cold rotary swaged tungsten heavy alloy, Mater. Sci. Eng. A 704 (2017) 25–31.
[10] W.M. Gan, Y.D. Huang, R. Wang, G.F. Wang, N. Hort, Microstructures and mechanical properties of pure Mg processed by rotary swaging, Mater. Des. 63 (2014) 83–88.
[11] H. Alkhazraji, E. El-Danaf, M. Wollmann, L. Wagner, Enhanced fatigue strength of commercial pure Ti processed by rotary swaging, Adv. Mater. Sci. Eng. (2015) 201837.
[12] W. Pachla, M. Kulczyk, S. Przybysz, J. Skiba, K. Wojciechowski, M. Przybysz, K. Topolski, A. Sobolewski, M. Charkiewicz, Effect of severe plastic deformation realized by hydrostatic extrusion and rotary swaging on the properties of CP Ti grade 2, J. Mater. Proc. Technol. 221 (2015) 255–268.
[13] M.S. Wang, Y.F. Wang, A.H. Huang, L. Gao, Y.S. Li, C.X. Huang, Promising tensile and fatigue properties of commercially pure titanium processed by rotary swaging and annealing treatment, Materials 11 (2018) 2261.
[14] E.O. Hall, The deformation and ageing of mild steel: III discussion of results, Proc. Phys. Soc. B 64 (1951) 747–753.
[15] N.J. Petch, The cleavage strength of polycrystals, Iron Steel Inst. 174 (1953) 25–28.
[16] Y.Y. Chen, J.F. Nie, F. Wang, H.B. Yang, C.C. Wu, X.F. Liu, Y.H. Zhao, Revealing hetero-deformation induced (HDI) stress strengthening effect in laminated Al-(TiB2+TiC)p/6063 composites prepared by accumulative roll bonding, J. Alloy. Compd. 815 (2020) 152285.
[17] Y. Cao, Y.B. Wang, R.B. Figueiredo, L. Chang, X.Z. Liao, M. Kawasaki, W.L. Zheng, S.P. Ringer, T.G. Langdonc, Y.T. Zhu, Three-dimensional shear-strain patterns induced by high-pressure torsion and their impact on hardness evolution, Acta Mater. 59 (2011) 3903–3914.
[18] W. Pachla, M. Kulczyk, M.S. Ryszkowska, A. Mazur, K.J. Kurzydlowski, Nanocrystalline titanium produced by hydrostatic extrusion, J. Mater. Proc. Technol. 205 (2008) 173–182.
[19] D.K. Yang, P.D. Hodgson, C.E. Wen, Simultaneously enhanced strength and ductility of titanium via multimodal grain structure, Scr. Mater. 63 (2010) 941–944.
[20] J. Kawałko, P. Bobrowski, P. Koprowski, A. Jarzębska, M. Bieda, M. Łagoda, K. Sztwiertnia, Microstructure evolution of CP titanium during deformation in KoBo process followed by cold rolling, J. Alloy. Compd. 707 (2017) 298–303.
[21] Y.C. Wan, B. Tang, Y.H. Gao, L.L. Tang, X.Y. Guo, Y.H. Zhao, Bulk nanocrystalline high-strength magnesium alloys prepared via rotary swaging, Acta Mater. 200 (2020) 274–286.
[22] D.A. Hughes, N. Hansen, D.J. Bammann, Geometrically necessary boundaries, incidental dislocation, Scr. Mater. 48 (2003) 147–153.
[23] H.J. Gao, Y.G. Huang, Geometrically necessary dislocation and size-dependent plasticity, Scr. Mater. 48 (2003) 113–118.
[24] D. Jorge-Badiola, A. Iza-Mendia, I. Gutiérrez, Study by EBSD of the development of the substructure in a hot deformed 304 stainless steel, Mater. Sci. Eng. A 394 (2005) 445–454.
[25] Y.J. Chen, Y.J. Li, J.C. Walmsley, S. Dumoulin, P.C. Skaret, H.J. Roven, Microstructure evolution of commercial pure titanium during equal channel angular pressing, Mater. Sci. Eng. A. 527 (2010) 789–796.
[26] M.H. Yoo, C.T. Wei, Slip modes of hexagonal-close-packed metals, J. Appl. Phys. 38 (1967) 4317–4322.
[27] M.H. Yoo, Slip, twinning, and fracture in hexagonal close-packed metals, Metall. Trans. A 12 (1981) 409–418.
[28] J.W. Christian, S. Mahajan, Deformation twinning, Prog. Mater. Sci. 39 (1995) 1–157.
[29] Z.W. Huang, S.B. Jin, H. Zhou, Y.S. Li, Y. Cao, Y.T. Zhu, Evolution of twinning systems and variants during sequential twinning in cryo-rolled titanium, Int. J. Plast. 112 (2019) 52–67.
[30] Y.T. Zhu, X.Z. Liao, X.L. Liao, Deformation twinning in nanocrystalline materials, Prog. Mater. Sci. 57 (2012) 1–62.
[31] F. Benmessaoud, M. Cheikh, V. Velay, V. Vidal, H. Matsumoto, Role of grain size and crystallographic texture on tensile behavior induced by sliding mechanism in Ti-6Al-4V alloy, Mater. Sci. Eng. A 774 (2020) 138835.
[32] X.P. Wu, S.R. Kalidindi, C. Necker, A.A. Salem, Prediction of crystallographic texture evolution and anisotropic stress–strain curves during large plastic strains in high purity a-titanium using a Taylor-type crystal plasticity model, Acta Mater. 55 (2007) 423–432.
[33] S.V. Zherebtsov, G.S. Dyakonov, A.A. Salem, S.P. Malysheva, G.A. Salishchev, S.L. Semiatin, Evolution of grain and subgrain structure during cold rolling of commercial-purity titanium, Mater. Sci. Eng. A 528 (2011) 3474–3479.
[34] J. Kawałko, M. Bieda, K. Wierzbanowski, D. Wojtas, W. Pachla, M. Kulczyk, Microstructure of titanium on complex deformation paths: comparison of ECAP, KoBo, and HE techniques, Mater. Charact. 141 (2018) 19–31.
[35] G.S. Dyakonov, S. Mironov, I.P. Semenova, R.Z. Valiev, S.L. Semiatin, Microstructure evolution and strengthening mechanisms in commercial-purity titanium subjected to equal-channel angular pressing, Mater. Sci. Eng. A 701 (2017) 289–301.
[36] G. Purcek, G.G. Yapici, I. Karaman, H.J. Maier, Effect of commercial purity levels on the mechanical properties of ultrafine-grained titanium, Mater. Sci. Eng. A 528 (2011) 2303–2308.
[37] D.V. Gunderov, A.V. Polyakov, I.P. Semenova, G.I. Raab, I.V. Alexandrov, N.A. Enikeev, R.Z. Valiev, Evolution of microstructure, macrotexture and mechanical properties of commercially pure Ti during ECAP-conform processing and drawing, Mater. Sci. Eng. A 562 (2013) 128–136.